Controlled Nanoscale Cracking of Graphene Ribbons by Polymer Shrinkage

Anjishnu Sarkar,[†] *Debadrita Paria,*[‡] *Ishan Barman,*[‡,†,▽] *David H. Gracias*[†,∥,§,*]

[†]Department of Chemical and Biomolecular Engineering, Johns Hopkins University. 3400 North Charles Street, Baltimore, MD 21218, United States.
[‡]Department of Mechanical Engineering, Johns Hopkins University. 3400 North Charles Street, Baltimore, MD 21218, United States.
[∥] Department of Materials Science and Engineering, Johns Hopkins University. 3400 North Charles Street, Baltimore, MD 21218, United States.
[§]Department of Chemistry, Johns Hopkins University. 3400 North Charles Street, Baltimore, MD 21218, United States.
[†]Department of Oncology, and [▽]The Russell H. Morgan Department of Radiology and Radiological Science, The Johns Hopkins University School of Medicine, Baltimore, Maryland 21287, United States

*Corresponding author: dgracias@jhu.edu

ABSTRACT

Controlled cracking of two-dimensional layered materials (2DLMs) can dramatically alter their crystallographic orientation, energy band gap, sheet resistance, and phonon softening. Previously, graphene has been ruptured using a variety of methods such as substrate mediated deformation or by using nanoscale probes. However, large-area, tunable nanoscale cracking in dry, suspended, and micropatterned graphene has yet to be demonstrated. Here, we describe a method to crack photolithographically patterned ribbons of graphene in a controlled manner. We first micropattern and suspend arrays of rectangular patterned graphene ribbons across topographically patterned lines of SU8 and generate controlled cracks by tunable shrinkage of SU8 using electron beam irradiation. We utilize a statistical design of experiments (DOE) to identify that two variables, namely the extent of prior ultraviolet SU8 crosslinking and the irradiated electron beam dose, contribute most significantly to the nano to microscale breakage of the micropatterned graphene ribbons. Also, the extent of nanoscale breakage in graphene can be tuned by varying the aforementioned factors. We anticipate that this approach can allow for integrated 2DLM based electronic and optical devices with engineered defects or break junctions.

Keywords: 2D layered materials, mechanically controlled break junctions, strain engineering, molecular junction, autoperforation

1. INTRODUCTION

While pristine graphene is impermeable,[1] when punctured or broken, graphene can develop unique magnetic,[2] electronic,[3] and chemical properties,[4-5] which can largely be attributed to the formation of dangling bonds,[6-7] point defects,[8] and Stone-Wales reconstruction of broken edges.[9] Importantly, the type, size, and doping of broken edges as well as environmental factors are important in determining their properties. The existence of cracks can increase the sheet resistance of graphene by a factor of two.[10] Of intellectual significance, as a nanoscale crack is formed, two layers of graphene slide on each other, resulting in periodic quantum oscillations. This phenomenon can be used to fabricate quantum interference devices with tunable conductance.[11] Due to the dramatic change in properties, controlled breakage and deformation of two-dimensional layered materials (2DLMs) opens up new applications such as nanopore devices for DNA translocation,[12] tunneling junctions,[13] subnanometer membranes for selective desalination and separation of gases,[14-15] nano biosensors,[16] two terminal memristive transistors,[17] strain sensors,[18] field effect biosensors,[19] electromagnetic interference shields,[20] locomoting devices,[21] storage devices,[5] and terahertz nanoantennas.[22] The ability to control the formation and propagation of defects in graphene is essential to design nanometer scale devices and composite polymers.[23-24]

Of relevance to chemical separations, dangling bonds in graphene nanoribbons have reactive zigzag edges,[25] and researchers have reported enhanced chemical reactivity around defects of graphene nanoribbons.[4] Such defects are crucial in molecular separations. Researchers have done calculations to show that dangling bonds in graphene pores can be engineered or chemically doped to develop molecular sieves to separate small molecules such as hydrogen from nitrogen and methane.[14, 26] Also, pores in graphene are not as easily contaminated as those in metallic (e.g.,

platinum or palladium) membranes,[27] and can enhance gas separation selectivity by six orders of magnitude as compared to silica membranes.[14]

Of relevance to sensors and electromagnetic devices, researchers have developed strain-pressure sensors with enhanced flexibility using a bimorph of graphene oxide and Ecoflex.[18] Caneva *et al*. developed mechanically controlled break junctions (MCBJs) by manually bending a graphene-polymer bilayer to the point of rupture.[28] They further demonstrated Fabry-Pérot like interference of electron waves at the edge of two sliding graphene layers, manifested by large amplitude, periodic oscillations in conductance at room temperature.

There are several methods to break 2DLMs in a controlled manner, such as with a focused ion beam,[7, 29] nanometer scale probe,[7, 30-32] and with the assistance of substrate mediated deformation with the underlying surface.[22] For example, Ci *et al*. developed nickel nanoparticle based knives by annealing a composite of nickel chloride and cleaved highly ordered pyrolytic graphite (HOPG) in a hydrogenated furnace at 500 ºC.[30] Further, they concluded that the crystallographic orientation of the incisions was governed by a threshold nanoparticle size of 10 nm. Campos *et al*. repeated the experiments with few-layered graphene (FLG) and reported the formation of 10 nm thick graphene ribbons with unique crystallographic alignment upon etching with Nickel nanoparticles.[31] Zhang *et al*. punctured 500 nm pre-cracks by a focused ion beam and used a nanoindenter to break 3 μm wide suspended graphene sheets.[33] Alternatively, researchers have tuned the size of nanopores in pre-cracked, suspended graphene sheets using oxidative etching, which is also highly relevant to nanofiltration and separations.[23] In terms of substrate mediated deformation, Liu *et al*. reported the formation and propagation of cracks while lifting off polystyrene beads sandwiched between two sheets of single-layer graphene, and fabricated two terminal memristive devices with biosensing capabilities.[17] Won *et al.* described a crack

lithography process by applying tensile stress on a double-layered graphene sheet sandwiched between alumina and polyimide substrates.[22] Graphene nano-slits were formed upon further evaporation of metal, which led to the fabrication of terahertz antennas.

Prior 2DLM cracking methods have their advantages and disadvantages. For probe induced breakage, it is difficult to control and isolate selective factors that trigger breakage over a diverse range of sizes. Alternatively, for substrate mediated deformation, the properties of the 2DLM are influenced by the underlying substrate. Also, a majority of the methods to deform 2DLMs utilize liquid solvents and involve capillary forces, which increases the susceptibility of the structures to collapse upon drying. Suspended 2DLMs are suitable for investigating tunable breakage to 3D architectures, as the free-standing 2DLMs can be easily deformed,[34] and yet, the physical and chemical properties of the 2DLMs are not significantly influenced by the underlying surface. Caneva *et al*.'s work on graphene based MCBJs highlights the possibilities of harnessing graphene breakage in characterizing quantum interference.[28]

All the above reasons directed us to develop and prescribe a platform to generate *in situ* nano to microscale breakage of suspended 2DLMs without the need for manual intervention. Here, we report a new method to induce *in situ* cracks in suspended graphene microribbons in the dry state. We suspended graphene microribbons on SU8 lines in an oblique fashion and observed controlled shrinkage of the SU8 lines, accompanied by an increase of the SU8 channel width and breakage of suspended graphene ribbons. We employ a statistical design of experiments (DOE) to investigate the effect of important process factors, including ultraviolet (UV) crosslinking, anisotropic annealing on a hotplate, and electron beam (e-beam) dose. Since our graphene patterns are suspended and not directly attached to a substrate, they represent attractive platforms for

developing break junctions and unique states of carbon, especially in the dry state, including vacuum.

2. MATERIALS AND METHODS

2.1. Substrate fabrication: We spin coated SU8 2005 on a silicon (Si) wafer at an angular speed of 4000 rpm. Next, we soft baked the photoresist for three minutes at 95 ºC. We photopatterned with four different UV intensities, namely 50 mJ/cm^2, 85mJ/cm^2, 125 mJ/cm^2, and 150 mJ/cm^2. We followed the exposure and development step with a hard bake for a period of 10 min at 150 ºC. After the hard bake, we treated the patterned SU8 with a brief low-power oxygen plasma (Plasma Etch Inc., Carson City, NV, USA; model no. PE-100, 60 W) for one minute.

2.2. Micropatterning of graphene: We purchased chemical vapor deposited (CVD) graphene grown on a copper foil from Graphene Laboratories Inc. (Ronkonkoma, NY, USA). Next, we transferred the CVD graphene to a thermal oxide (290 nm) coated Si wafer, which was purchased from NanoSilicon, Inc. (San Jose, CA, USA). We spin coated polymethylmethacrylate (PMMA, M_w~996,000) at 4000 rpm and soft baked the copper foil at 85ºC for 15 minutes, followed by heating it at 135 ºC for another 15 minutes. Next, we etched the graphene using 1 M iron chloride ($FeCl_3$) at room temperature. We purchased the chemicals from Sigma-Aldrich (St. Louis, MO, USA). Then, we washed the PMMA-CVD graphene bilayer with water and transferred it to the thermal oxide coated Si wafer. Finally, after drying the film, we dissolved the PMMA in acetone for 6 hours. The detailed steps are tabulated in Figure S1.

We photolithographically micropatterned ribbons of CVD graphene (microribbons) on the oxidized Si substrate. We used two array dimensions, 3 μm microribbons with 3 μm spacing and 5 μm microribbons with 8 μm spacing. We spin coated a positive photoresist, namely S1818 (Kayaku Advanced Materials, Inc., Westborough, MA, USA) at an angular speed of 4000 rpm and

soft baked the film at 110 ºC for 1 minute. We used a UV crosslinking intensity of 150 mJ/cm^2 to pattern the samples and developed the micropatterned graphene with MF 319 developer for 30 s. We then etched the exposed graphene samples with oxygen (O_2) plasma (RF 60 W, t = 30 s). Finally, we immersed the samples in acetone to dissolve the photoresist and expose the graphene microribbons.

2.3. Transfer of micropatterned graphene: We spin coated a transfer layer of PMMA on the photopatterned array of CVD graphene microribbons on the oxide coated Si wafer. We etched the underlying thermal oxide with an aqueous solution of 1M potassium hydroxide (KOH) to release the microribbons along with the PMMA layer. We washed the PMMA-micropatterned graphene samples several times with deionized (DI) water and placed them on top of SU8 lines. During the transfer, we transferred the array of graphene microribbons in such a way that the microribbons were aligned at an angle of approximately 45º with respect to the SU8 lines. We chose this angle since a 45º results in asymmetry at the line edge of contact. Also, parallel transfer (~0º) resulted in extensive breakage during transfer itself, while perpendicular transfer (~90º) was not explored since the contact line has no asymmetry.

We dried the samples for 24 hours and then dissolved the PMMA with acetone. We observed the best results when the samples were dried using critical point drying (Tousimis 795 Rockville, MD, USA) or hexamethyldisilazane (HMDS) as a low surface tension alternative solvent to water.[35] This choice has been successfully employed in the past without any reported breakage in suspended graphene sheets,[36] and reduces drying time, which minimizes SU8 swelling. After the transfer and removal of PMMA, we annealed the samples on a hotplate set at 200 ºC for a period of 10 minutes. We use bright field optical micrographs and isometric SEM images of

graphene microribbons to confirm suspended structures and Raman spectra to confirm crack-free graphene microribbons on SU8 lines (Figure S2).

2.4. Electron beam assisted breakage of graphene: We sputter coated gold (Au) on the samples to enhance contrast in scanning electron microscopy (SEM) and subsequently placed the samples in an SEM. We used a tungsten filament thermionic emission JEOL JSM IT100 SEM and three different levels for the e-beam dose, namely low, medium (med) and high. The magnitude of the e-beam dose was determined by the probe current, the duration of exposure and the area of the sample under the e-beam. We further approximated the e-deam dose for each level by measuring the probe current with a Faraday cup (Details in SI and Figure S3). We estimate that the low e-beam dose corresponds to a charge per unit area less than 0.5 mC/cm^2, the med e-beam dose corresponds to charge per unit area of approximately 366 mC/cm^2 and the high e-beam dose corresponds to charge per unit area greater than 915.1 mC/cm^2.

2.5. Raman spectroscopy: We used an XploRA PLUS Raman microscope (HORIBA Instruments Inc., Edison, NJ, USA) to acquire the Raman spectra. We used a 532 nm diode incident laser and a 100x objective (MPlan N, Olympus, Center Valley, PA, USA) to focus the laser beam on the sample and a thermoelectrically cooled charge-coupled device (CCD) camera (1024X256-OE Syncerity, HORIBA Instruments Inc., Edison, NJ, USA) to collect the scattered spectra. After the spectral acquisition, we post-processed the spectra for background removal and scaled the data to normalize the integration time of acquisition.

3. RESULTS AND DISCUSSIONS

Over the past decade, researchers have investigated a variety of approaches for suspending graphene sheets on various periodic structures, including using metallic bars and holey Carbon based quantifoil grids.[37-39] Takamura *et al*. suspended graphene sheets on SU8 and demonstrated

that the lateral shrinkage leads to a tensile strain that acts within a two micron width of the resist.[40] While it was proposed that additional strain could result in the nanoscale breakage of graphene, no well-defined correlation has been reported to our knowledge, which quantifies the extent of breakage.

We illustrate the procedure of transfer and graphene breakage in Figure 1a. During imaging of the sample under an e-beam, we discovered cracks forming predominantly near the interface of the graphene microribbons and the SU8 lines (Figures 1b and c). The cracks are typically directed at an angle of 94.8º±9.0º to the length of the graphene microribbon. We observe that the range of the width of the crack was approximately 105±30 nm at the interface of graphene-SU8, and as the crack propagates in the otherwise pristine, suspended graphene, it tapers to a width of around 100 nm. It is interesting to note that as the cracks do not necessarily extend to the other edge of the suspended graphene, there are areas in the graphene which have a crack with a width of 0-100 nm. The significance of the formation and propagation of cracks in our methodology is that it doesn't require manual bending of the SU8-graphene system, as was previously found.[28] Also, the nanoscale breakage can be observed in large-area devices and can be potentially scaled to wafer sized applications.

The absence of a bandgap in graphene allows broadband electronic absorption and the Raman spectra encodes information on both atomic structures and electronic properties of graphene.[41,42] Raman spectroscopy also offers an excellent tool for monitoring the effect of various external factors like doping, chemical modification, structural damage, and mechanical interventions on optical and electronic properties of graphene. To gain better insight into the effect of cracking in our suspended graphene, we acquired Raman spectrum of the suspended region and compared it to the one supported on the SU8 structures. The two spectra in Figure 1d are offset for

the purpose of visualization. We observe shifts in the peak positions for both G and 2D peaks in the spectra acquired from the suspended, cracked graphene as compared to that of the supported, crack-free graphene.

Furthermore, we observe the peaks for the cracked graphene to be broader with a highly diminished 2D peak. Tian *et al.* have reported similar observations during laser mediated asymmetric patterning of suspended graphene.[43] This reduction in intensity can be attributed to the complex interplay between doping due to the presence of impurities,[44] and strain due to suspension,[45] both of which have been reported to play a significant role in the position and width of G and 2D.[46-47] But a key observation is the appearance of a prominent disorder peak, known as the D peak, in the spectrum of the unsupported graphene, which is absent in the supported region. This confirms the appearance of cracks in the suspended region and indicates that the unsupported region is more prone to cracking. We note that to enhance contrast and reduce e-beam charging we deposited a thin layer of gold (Au) on the microribbons prior to SEM imaging and Raman measurements. Prior literature reports indicate that Au deposited on monolayer graphene coalesces, presumably, around contamination sites.[48-49] Further studies are needed to thoroughly understand the role of the deposited Au in the process and Raman spectra.

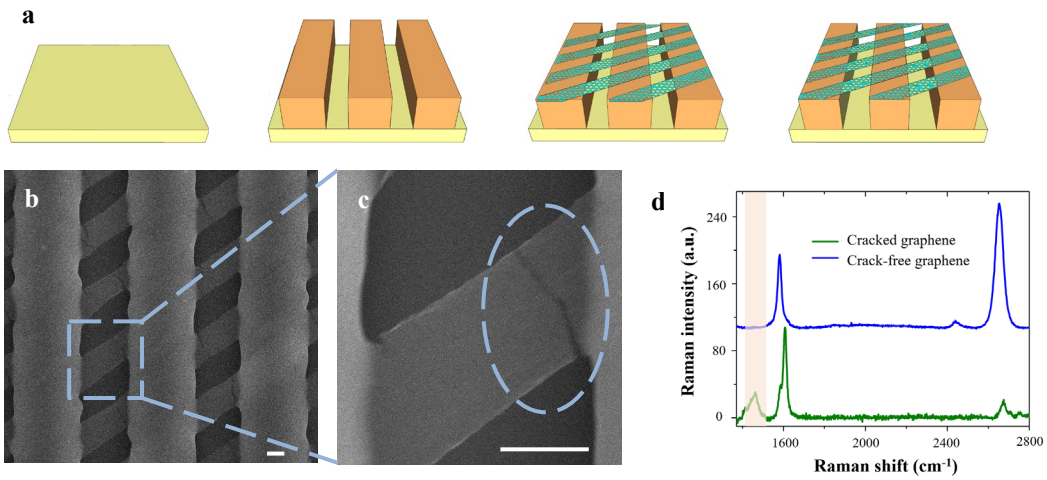

Figure 1. Illustration of nanoscale graphene breakage and Raman characterization. (a) Schematic illustration of the overall process to pattern SU8 lines, transfer micropatterned graphene, and controlled cracking. (b) Representative SEM micrograph of 3 μm graphene microribbons on 8 μm SU8 lines with 5 μm channel width. (c) Zoomed-in image of a cracked microribbon on SU8 processed at 150 mJ/cm^2. (d) Raman spectra collected on supported and crack-free graphene (blue) and suspended, cracked graphene (green). The shaded pink region indicates a prominent D peak in the spectrum of the cracked graphene. The scale bars in panel (b) and (c) represent 2 μm.

To elucidate a mechanism for cracking, we systematically investigated the effect of e-beam dose at different photocrosslinking intensities, processing conditions and e-beam dose. Since we wanted to quantify the extent of cracking, we decided to increase the field of view to 350 μm^2 and the width of the graphene microribbons to 5 μm. The SEM micrographs show that a rise in the e-beam dose for a given UV crosslinking intensity (50 mJ/cm^2) causes a widening in the channels between two adjacent SU8 lines, and consequently, the extent of cracking in a single graphene microribbon (Figure 2). We measure the extent of cracking in a single graphene microribbon, termed as percentage of graphene cracking, by calculating the ratio of the measured crack length perpendicular to the graphene microribbon after e-beam exposure to the overall width of the graphene microribbon (i.e. 5 μm) prior to e-beam exposure. For the med e-beam dose, a narrow

slit is formed in the microribbon with a thickness of 150±30 nm and an area of 0.5±0.2 μm^2. We found that for the high e-beam dose, the graphene undergoes out of plane buckling, which causes the length of the slit to remain invariant, while the slit widens. Since the percentage of graphene cracking was reported based on the slit length, the percentage doesn't change as the e-beam dose is increased from med to high. We note that the area of cracked graphene for the high e-beam dose (3.6±0.2 μm^2) surpasses that of the med dose (0.5 μm^2) by a factor of seven. We found that the percentage rise in SU8 channel width and graphene cracking respectively reached a value of 15.9% and 72.1% at the highest e-beam dose. We note that while the reported percentage of graphene cracking corresponds to that measured on one microribbon, we observe similar percentage breakage for other graphene microribbons of the same dimensions, when irradiated with the same e-beam dose (Figure S4).

SU8 is a widely used resist responsive to UV radiation,[50-52] focused e-beams,[53-55] deep X-ray lithography,[56] and femtosecond two-photon absorption.[57] Commercially available SU8 contains an octaglycidylic ether of a condensation product derived from Bisphenol A,[58-59] and an acidic photoinitiator,[51] which is responsive to both UV light and e-beam. It has been suggested that an e-beam could lead to the protolysis of the photoinitiator, which leads to the formation of carbonium ions,[57] and consequently, the protonation of the oxygen atom of the epoxy group.[60] Electron beam lithography at low intensities is accompanied by proximity effect,[61] in which the incident, as well as the backscattered electrons, affect the absorbed radiation at a certain resist depth. Glezos *et al*. proposed a reaction-diffusion model to characterize the proximity effect of an e-beam, wherein the diffusion coefficient corresponding to the diffusion of the photoinitiator in the polymer was found to be a decreasing function of the resist depth.[62] Sarkar *et al*. demonstrated that the interplay of the diffusion coefficient and the gradient of the photoinitiator concentration

results in the broadening of the sidewalls for isolated SU8 lines.[60] Elsewhere, Denning *et al*. demonstrated that holographic exposure of SU8 could lead to the removal of the loosely held oligomers in the crosslinked network, which results in shrinkage of SU8 structures.[63]

We believe that SU8 exposed to 50 mJ/cm^2 UV irradiation results in partially crosslinked oligomer units, and the SU8 subsequently shrinks in response to the proximity effect of the 20 KV e-beam. Since SU8 lines have a length of 3 mm and a width of 5 μm, we hypothesize that the SU8 should expand along the 3 mm length. However, the SU8 lines are attached to the Si substrate; hence, to maintain the original volume upon expansion, the SU8 lines should decrease in width. To the best of our knowledge, this is the first time that the shrinkage of partially photophatterned SU8 lines with an e-beam has been systematically studied and reported.

We also investigated other factors that could potentially influence the breakage. We hypothesized that heating the graphene-SU8 system on a hotplate could induce anisotropicity in the system and result in a strain in the graphene-SU8 interface. For the same UV crosslinking intensity (50 mJ/cm^2), we studied the evolution of SU8 channel width for two different heating temperatures (T=90 ºC, T=200 ºC) in comparison to that of a counterpart without heating (Figure 2b). For SU8 photopatterned with a UV crosslinking intensity of 50 mJ/cm^2, we observe that SU8 channel width increases by a factor of 16 % on heating. The SU8 lateral dimension decreases with heat, and thus the spacing increases with the temperature.

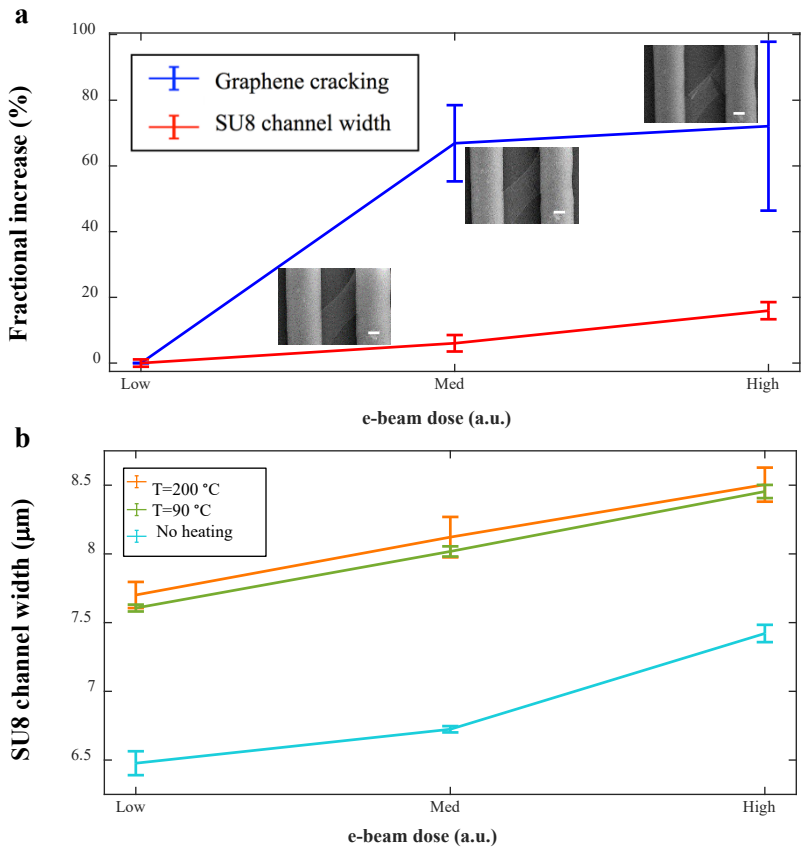

Figure 2. Electron beam mediated increase in SU8 channel width and nanoscale breakage in graphene microribbons. (a) Fractional increase in graphene cracking (blue) and SU8 channel width (red), is plotted for three progressively increasing values of e-beam dose. SEM micrographs (scale bar 2 μm) taken at three e-beam doses show that a crack-free, suspended graphene microribbon (no cracks, low e-beam dose) develops a crack at the SU8: graphene interface (med e-beam dose) and additional nanoscale breakage at high e-beam dose. (b) Rise in SU8 channel width with e-beam doses for no heating (blue), heating at 90 ºC (green), and heating at 200 °C (orange). We patterned the SU8 lines with a UV crosslinking intensity of 50 mJ/cm^2.

We carried out statistical analysis to gain a better understanding of the mutual interplay of the three factors. In addition to UV SU8 photocrosslinking and the e-beam dose, we investigated the effect of anisotropic hotplate annealing. We chose the rise in SU8 channel width and the percentage of cracking as response parameters. Next, we conducted an L9 Taguchi design comprising nine experiments (three factors and three levels) to study the effects of UV SU8 crosslinking, e-beam dose, and the effect of anisotropic hotplate annealing (Table 1).[64-65]

We calculated the statistical mean and standard deviation using JMP software and plotted the results with MATLAB. We observe that the SU8 channel width decreases with increasing UV crosslinking, increases with increasing e-beam dose, and has a mixed effect with heating (Figure 3a). We compared the mutual contribution of each factor for a given response parameter by comparing the negative logarithm of the p-values. The DOE indicated that SU8 channel width was most sensitive to the extent of UV crosslinking (Figure 3b).

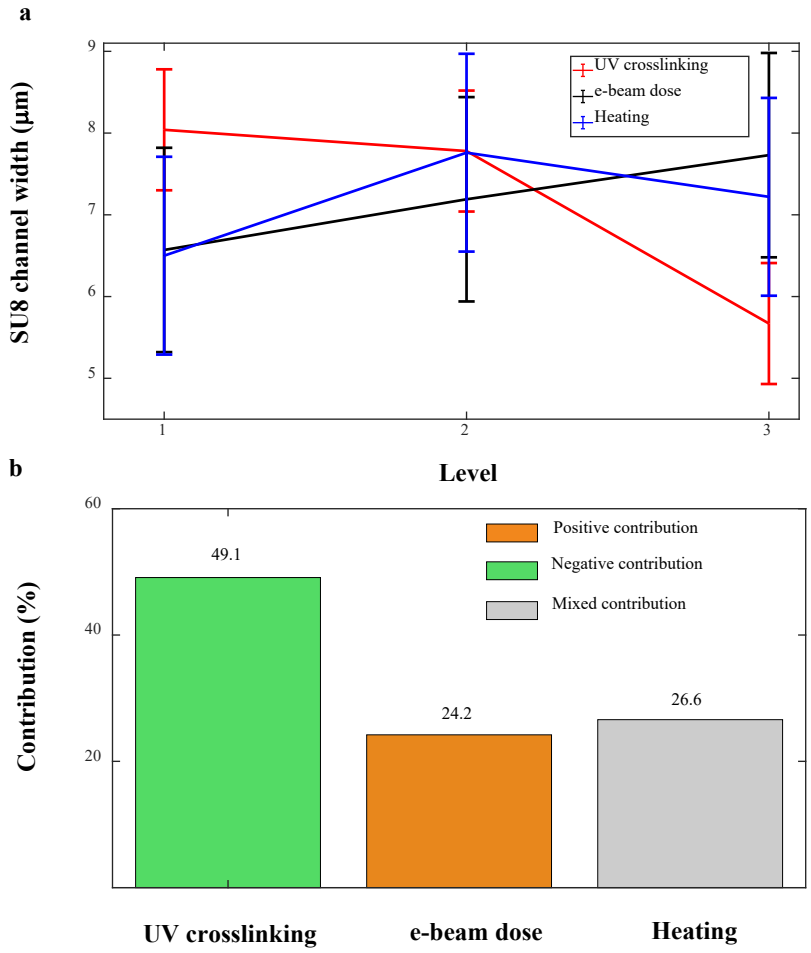

Figure 3. Analysis of the influence of three factors on SU8 channel width. (a) Taguchi analysis showing the effect of UV crosslinking, e-beam dose, and heating. (b) Relative magnitudes of contribution for each factor

We rationalize our results as follows. Although UV radiation and e-beam individually result in growth in the polymer chain by polymerization,[66] each factor has a distinct effect on the

micrometer scale dimensions of SU8. When crosslinked with UV intensities lower than the prescribed value, SU8 doesn't entirely polymerize and partially UV crosslinked SU8 (intensities 50 mJ/cm^2, 85 mJ/cm^2) has a smaller line width as compared to completely UV crosslinked SU8 (125 mJ/cm^2). As a result, SU8 UV crosslinked with 50 mJ/cm^2 has the smallest line width and consequently, the highest channel spacing. Our findings are consistent with those of Ling *et al*., in which a rise in SU8 dimensions was observed with higher UV crosslinking intensities.[66-67]

The effect of annealing has a mixed contribution on SU8 channel width. The width of the SU8 lines increased with increasing UV photocrosslinking intensity, and thus, the SU8 channel width dropped. We expected the e-beam to cause elongation along the length of the SU8 channels, and consequently, shrinkage in width. Also, the e-beam irradiation could cause crosslinking at the apex of the SU8 channels, and consequently, a rise in the local density of the resist. Thus, the SU8 channel width was expected to increase with a rise in the e-beam dose (Figure 2). Hence, our results are consistent with our predictions.

We believe that the rise in SU8 channel width is a latent factor that subsequently results in the breakage of graphene. While e-beam dose has a positive contribution, the effect of annealing and UV photocrosslinking have negative and mixed contributions on graphene cracking, respectively.

Although UV radiation and e-beams individually result in growth in the polymer chain,[66] each factor has a distinct effect on the micrometer scale dimensions of SU8. Ling *et al*. showed that isolated microstructures of SU8 irradiated with higher UV intensities undergo a higher degree of polymerization, which results in a rise in the lateral dimensions.[67]

We rationalize that heating on a hotplate causes the partially UV crosslinked oligomers to shrink, resulting in a drop in the SU8 line width and an increase in the SU8 channel width. A

similar occurrence of resist shrinkage in SU8 has been observed with isotropic annealing in a furnace,[66] or caused by capillary forces encountered during resist development.[67] The higher sensitivity of SU8 shrinkage to UV and e-beam processes as compared to heating indicate that the mechanism of shrinkage is electron/ free-radical mediated. We believe that the rise in SU8 channel width is a latent factor that subsequently results in the nanoscale breakage of graphene.

We also carried out a comparative study of the effect of each factor on the extent of graphene cracking. While e-beam dose has a positive contribution on graphene cracking, heating and UV crosslinking have negative and mixed contributions, respectively (Figure 4a). Among the three factors, UV crosslinking has the highest mutual contribution on the percentage of graphene cracking (Figure 4b). The DOE analysis as shown in Table 1 revealed that the permutations of the factors corresponding to experiment 4 (85 mJ/cm^2, no heating, med e-beam dose) and experiment 5 (85 mJ/cm^2, 90 ºC, high e-beam dose) resulted in statistically significant cases of cracking. The salient feature of both the permutations is a UV crosslinking intensity of 85 mJ/cm^2.

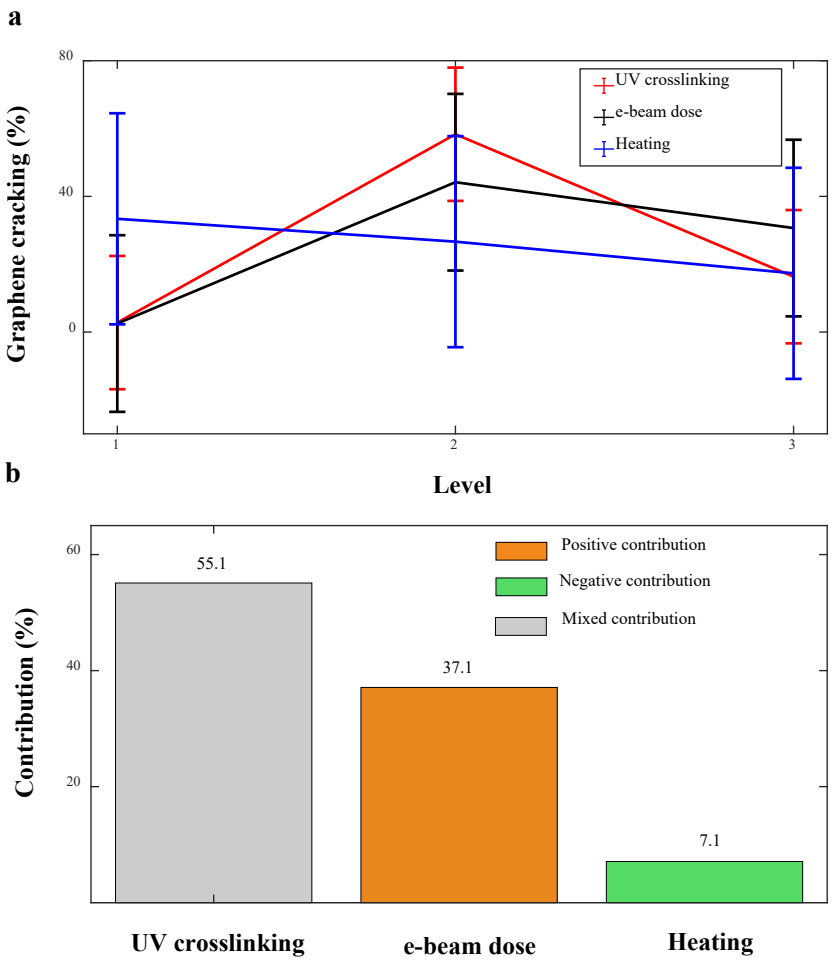

Figure 4. Investigation of the effect of three factors on graphene cracking. (a) Taguchi analysis showing the mean and standard deviations corresponding to UV crosslinking, e-beam dose, and heating. (b) Comparison of contribution for each factor.

We rationalize our results as follows. SU8 when photopatterned with UV crosslinking intensities of 50 mJ/cm^2 is mostly uncrosslinked while that with 125 mJ/cm^2 is fully crosslinked. The development of SU8 with UV crosslinking of 50 mJ/cm^2 results in partial removal of the undeveloped oligomers. In contrast, SU8 UV crosslinked with 85 mJ/cm^2 is partially polymerized. We always observed the cracks originating at the SU8: graphene interface (video S1), possibly due to the mismatch in mechanical properties and strain between SU8 and graphene at this interface. Also we anticipate that since SU8 is a negative photoresist, undercrosslinked SU8 would have a

high fraction of incompletely crosslinked oligomers at its line edges, where e-beam induced shrinkage would be significant. We believe that the non-uniformity in the roughness at high UV crosslinking leads to a strain in the graphene: SU8 interface as the manner of graphene transfer occurs in an aqueous medium. Subsequently, the e-beam irradiation causes the graphene microribbons to crack. Also, as opposed to annealing in a furnace, which is isotropic, heating on a hotplate results in temperature gradients, which could possibly lead to the breakage of graphene.

Unlike heating on a hotplate, which is influenced by thermal conduction and results in a lack of reproducibility due to variations in thermal properties of the substrate and heating process, UV crosslinking of SU8 is highly reproducible, controllable and tunable. Since UV crosslinking plays a dominant effect on both the response parameters, we can controllably and reproducibly manipulate the increase in the SU8 channel width and the extent of graphene cracking. It is noteworthy that our approach could be extended to sub-micron architectures with alternate deep UV sensitive resists like PMMA.[68]

Aside from the mean response, we calculated the signal-to-noise ratio (S/N) to understand the desirability of each factor. We used a larger-the better approach to calculate the signal-to-noise ratio using the following formula.

$$\frac{S}{N} = -10 \times log_{10} \frac{1}{n} \sum \left(\frac{1}{Y_l^2} \right)$$

where Y_l is the response for a factor l and n is the number of responses in the factor level combination. We note that our formula contains a prefactor of 10, and is consistent with the S/N ratios as calculated using standard statistical software (e.g. JMP14). We calculated the average S/N ratio for the set of nine experiments and compared it with the S/N ratio of each level.

For each response parameter, we plotted the S/N ratio against the average S/N ratio of all nine experiments (Figures 5 and 6). For SU8 channel width, the plot of S/N ratio decreases monotonically with UV SU8 crosslinking (maximum at 50 mJ/cm^2). An annealing temperature of 90 ºC resulted in the highest S/N ratio for SU8 channel width. We inferred the effect of each factor on SU8 channel width and graphene cracking (Figures 5 and 6, respectively). We report that UV crosslinking has a negative effect on SU8 channel width (Figure 5a). We observe that the e-beam dose has a positive effect on SU8 channel width (Figure 5b), while heating has a mixed effect (Figure 5c).

For graphene cracking, UV crosslinking has a mixed effect (Figure 6a), while e-beam dose and heating have positive (Figure 6b) and mixed (Figure 6c) effects, respectively. The Taguchi analysis as shown in Table 1 revealed that the permutations of the factors corresponding to experiment 4 (85 mJ/cm^2, no annealing, med e-beam dose) and experiment 5 (85 mJ/cm^2, 90 ºC, high e-beam dose) resulted in statistically significant cases of cracking. The characteristic feature of both the permutations is a UV SU8 crosslinking intensity of 85 mJ/cm^2.

The above trends strongly indicate that a rise in SU8 channel width and the subsequent cracking in suspended graphene microribbons is a direct consequence of the e-beam dose. As already established in Figure 4b, the temperature is not the dominating factor, which is in agreement with our findings that heating has mixed effects on both SU8 channel width and graphene cracking. We compare the relative robustness of each factor on a response parameter by measuring the difference of the maximum and minimum values of S/N ratios for that factor. As we follow a larger-the-better approach, the factor with the highest value of the difference in S/N ratio across levels has the maximum effect on the response parameter. We tabulate the difference of S/N ratios for each response parameter and assign ranks to allocate the relative importance of

each factor (Tables 2 and 3). We report that UV crosslinking has the highest influence on both the response parameters, which conclusively proves our findings in Figure 3b and 4b.

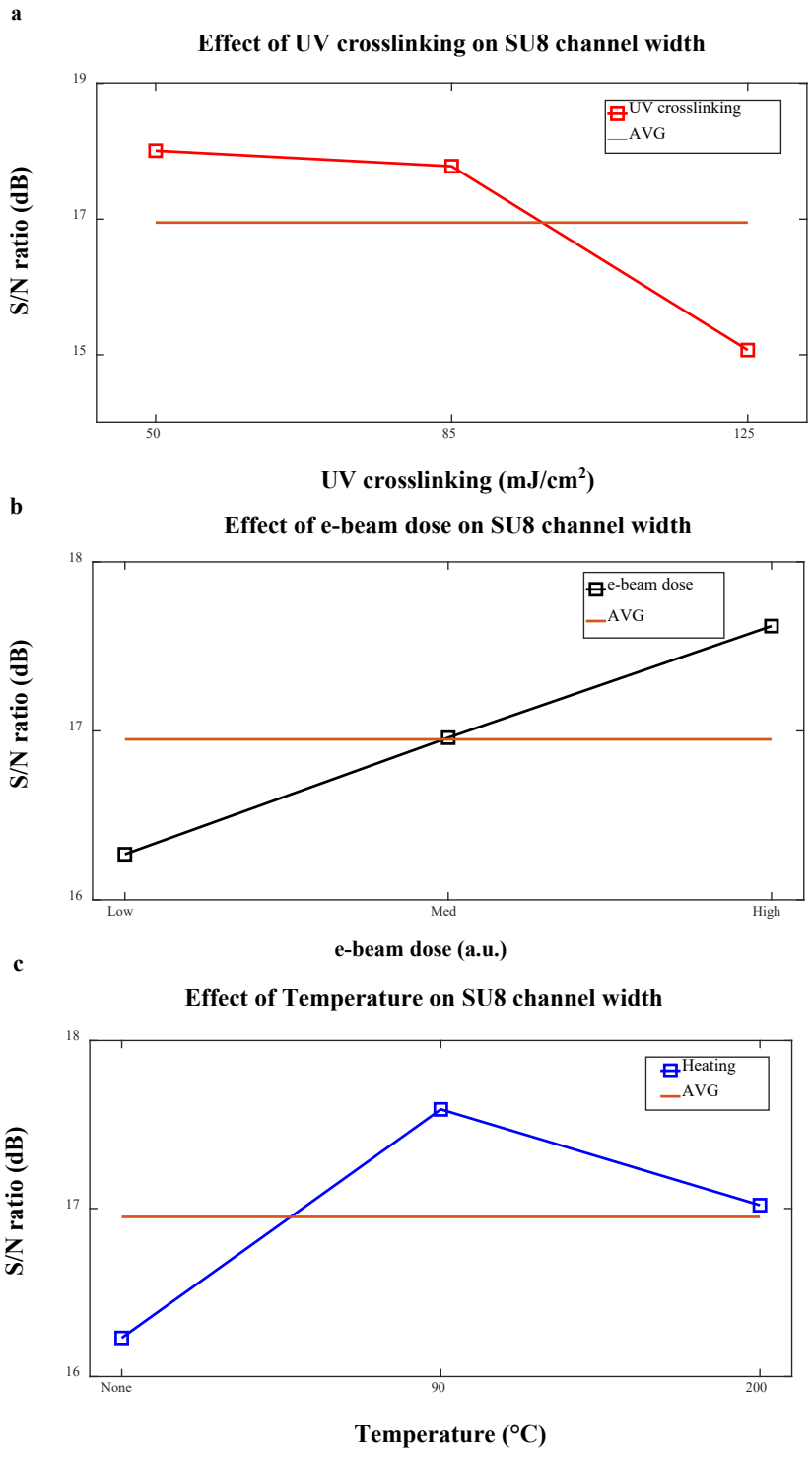

Figure 5. Determination of the robustness of the DOE for SU8 channel width. Comparison of signal-to-noise (S/N) ratios for each factor with the average S/N ratio for all nine experiments. Effect of, (a) UV crosslinking, (b) e-beam dose, and (c) heating on SU8 channel width. AVG indicates the average.

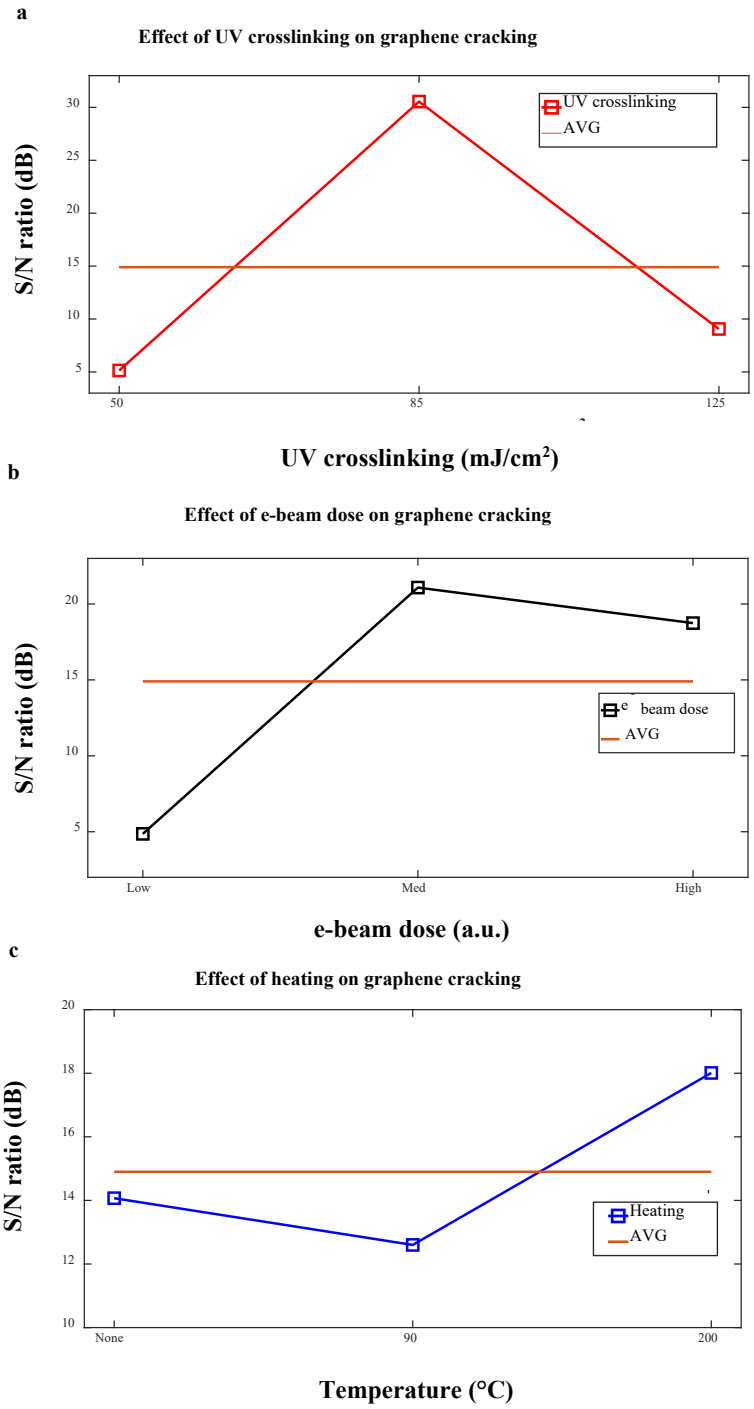

Figure 6. Determination of the robustness of the DOE for graphene cracking. Comparison of signal-to-noise (S/N) ratios for each factor with the average S/N ratio for all nine experiments. Effect of, (a) UV crosslinking, (b) e-beam dose, and (c) heating on graphene cracking. AVG indicates the average.

Table 1. Evolution of SU8 channel width and graphene cracking for nine sets of experiments

Parameters					
Experiment	Crosslinking (mJ/cm^2)	Temperature (°C)	e-beam dose (a.u.)	SU8 channel width (µm)	Graphene cracking (%)
1	50	No heating	Low	6.5±0.2	0.0±0.0
2	50	90	Med	9.0±0.1	0.0±0.0
3	50	200	High	8.5±0.5	6.3±2.0
4	85	No heating	Med	6.9±0.1	91.5±1.7
5	85	90	High	8.7±0.1	77.9±3.5
6	85	200	Low	7.6±0.1	5.5±1.0
7	125	No heating	High	5.9±0.1	7.6±9.4
8	125	90	Low	5.5±0.1	0.0±0.0
9	125	200	Med	5.5±0.0	40.0±40.4

Table 2. Comparative study of the effect of each factor on SU8 channel width

Comparison of the effect of each factor on SU8 channel width			
S/N ratio (dB)	Factors		
	UV crosslinking	e-beam dose	Temperature
Minimum	15.0	16.2	16.2
Maximum	18.0	17.6	17.6
Difference	2.9	1.3	1.4
Rank	1	3	2

Table 3. Comparative study of the effect of each factor on graphene cracking

Comparison of the effect of each factor on graphene cracking			
S/N ratio (dB)	Factors		
	UV crosslinking	e-beam dose	Temperature
Minimum	5.1	4.9	12.6
Maximum	30.6	21.1	18.0
Difference	25.4	16.2	5.4
Rank	1	2	3

4. CONCLUSION

In summary, we have developed a new strategy to induce tunable, *in situ* nanoscale cracks in suspended, single-layer patterned graphene microribbons. In our process, the breakage of graphene doesn't require any manual intervention or probes and can be scaled to wafer size devices for mechanically controlled break junctions. We implement several new ideas to controllably generate nano to micrometer scale cracks in single-layer graphene. First, by systematically varying the extent of SU8 crosslinking, temperature, and e-beam dose, we can induce up to 20 % shrinkage in SU8 lines and complete breakage of graphene microribbons in a controlled manner. We believe that the increase in SU8 channel width occurs by an e-beam/free radical mediated method, which acts as a latent parameter for graphene cracking. Second, we have observed that the degree of UV crosslinking in SU8 plays a major role in the phenomenon of graphene breakage. The significance of the finding is that nanoscale cracks in graphene can be induced in a facile and reproducible manner as the UV crosslinking intensity is easy to control, unlike the temperature on a hotplate as the latter is susceptible to thermal gradients and process as well as substrate dependent. As UV crosslinking is the dominant factor, this strategy can be reproducibly extended to other polymers and resists, which are simultaneously responsive to UV radiation and e-beam. Finally, we have established a systematic correlation between e-beam dose and the extent of nanoscale breakage in graphene. We anticipate that this approach can be used to create functional devices with cracked graphene, such as *in situ* break junctions and nanoengineered platforms for surface enhanced Raman scattering (SERS). We believe that this work could be combined with micro Raman spectroscopy to determine the fracture toughness of the broken, zig-zag edges of suspended graphene.[69] We also believe that this approach can be used to create new cracked forms of alternate 2D layered materials and ultrathin films.

ASSOCIATED CONTENT

Supporting Information

The Supporting Information (SI) is available free of charge on the ACS Publications website at DOI:

The SI includes: Fabrication and patterning schematics; crack-free, suspended graphene microribbons on micropatterned SU8 lines; determination of the best permutation for achieving highest SU8 channel width; determination of the absorption current corresponding to the e-beam doses "low", "med" and "high" using a Faraday cup; effect of e-beam dose on 5 μm wide graphene microribbons; control experiments: expansion of the SU8 channel width in the absence of graphene; nanoscale cracks developed in 8 μm wide, suspended graphene microribbons; note on the spread in the standard deviation of the response parameter.

AUTHOR INFORMATION

Corresponding Author

*E-mail: David Gracias; dgracias@jhu.edu

ORCID

Anjishnu Sarkar: 0000-0001-9691-5851

Debadrita Paria: 0000-0001-8251-4379

Ishan Barman: 0000-0003-0800-0825

David H. Gracias: 0000-0003-2735-4725

FUNDING

This work was supported by the Air Force Office of Scientific Research MURI (Multidisciplinary University Research Initiative) program (FA9550-16-1-0031) and the National Science Foundation (CMMI-1635443).

ACKNOWLEDGEMENTS

We thank Dr. Kenneth Livi and Mr. Phillip Chapman from the Department of Materials Science and Engineering, Johns Hopkins University for providing guidance with the installation of Faraday cup and the measurement of the e-beam dose. We thank Prof. Thomas Kempa from the Department of Chemistry, Johns Hopkins University for helpful discussions.

NOTES

The authors declare no competing financial interest.

REFERENCES

1. Bunch, J. S.; Verbridge, S. S.; Alden, J. S.; van der Zande, A. M.; Parpia, J. M.; Craighead, H. G.; McEuen, P. L., Impermeable atomic membranes from graphene sheets. *Nano Lett.* **2008,** *8* (8), 2458-2462.
2. Akhukov, M. A.; Fasolino, A.; Gornostyrev, Y. N.; Katsnelson, M. I., Dangling bonds and magnetism of grain boundaries in graphene. *Phys. Rev. B* **2012,** *85* (11), 115407.
3. Nakada, K.; Fujita, M.; Dresselhaus, G.; Dresselhaus, M. S., Edge state in graphene ribbons: Nanometer size effect and edge shape dependence. *Phys. Rev. B* **1996,** *54* (24), 17954-17961.
4. Wang, X.; Li, X.; Zhang, L.; Yoon, Y.; Weber, P. K.; Wang, H.; Guo, J.; Dai, H., N-Doping of Graphene Through Electrothermal Reactions with Ammonia. *Science* **2009,** *324* (5928), 768-771.
5. Olsson, E.; Hussain, T.; Karton, A.; Cai, Q., The adsorption and migration behavior of divalent metals (Mg, Ca, and Zn) on pristine and defective graphene. *Carbon* **2020,** *163*, 276-287.
6. Liu, Z.; Suenaga, K.; Harris, P. J. F.; Iijima, S., Open and closed edges of graphene layers. *Phys. Rev. Lett.* **2009,** *102* (1), 015501.
7. He, K.; Robertson, A. W.; Gong, C.; Allen, C. S.; Xu, Q.; Zandbergen, H.; Grossman, J. C.; Kirkland, A. I.; Warner, J. H., Controlled formation of closed-edge nanopores in graphene. *Nanoscale* **2015,** *7* (27), 11602-11610.
8. El-Barbary, A. A.; Telling, R. H.; Ewels, C. P.; Heggie, M. I.; Briddon, P. R., Structure and energetics of the vacancy in graphite. *Phys. Rev. B* **2003,** *68* (14), 144107.
9. Banhart, F.; Kotakoski, J.; Krasheninnikov, A. V., Structural defects in graphene. *ACS Nano* **2011,** *5* (1), 26-41.
10. Lee, J.; Kim, Y.; Shin, H.-J.; Lee, C.; Lee, D.; Lee, S.; Moon, C.-Y.; Lee, S. C.; Kim, S. J.; Ji, J. H.; Yoon, H. S.; Jun, S. C., Crack-release transfer method of wafer-scale grown graphene onto large-area substrates. *ACS Appl. Mater. Interfaces* **2014,** *6* (15), 12588-12593.
11. Gehring, P.; Thijssen, J. M.; van der Zant, H. S. J., Single-molecule quantum-transport phenomena in break junctions. *Nat. Rev. Phys.* **2019,** *1* (6), 381-396.
12. Schneider, G. F.; Kowalczyk, S. W.; Calado, V. E.; Pandraud, G.; Zandbergen, H. W.; Vandersypen, L. M. K.; Dekker, C., DNA translocation through graphene nanopores. *Nano Lett.* **2010,** *10* (8), 3163-3167.
13. Bellunato, A.; Vrbica, S. D.; Sabater, C.; de Vos, E. W.; Fermin, R.; Kanneworff, K. N.; Galli, F.; van Ruitenbeek, J. M.; Schneider, G. F., Dynamic Tunneling Junctions at the Atomic Intersection of Two Twisted Graphene Edges. *Nano Lett.* **2018,** *18* (4), 2505-2510.
14. Du, H.; Li, J.; Zhang, J.; Su, G.; Li, X.; Zhao, Y., Separation of Hydrogen and Nitrogen Gases with Porous Graphene Membrane. *J. Phys. Chem. C* **2011,** *115* (47), 23261-23266.
15. O'Hern, S. C.; Boutilier, M. S. H.; Idrobo, J.-C.; Song, Y.; Kong, J.; Laoui, T.; Atieh, M.; Karnik, R., Selective ionic transport through tunable subnanometer pores in single-layer graphene membranes. *Nano Lett.* **2014,** *14* (3), 1234-1241.
16. Jin, X.; Feng, C.; Ponnamma, D.; Yi, Z.; Parameswaranpillai, J.; Thomas, S.; Salim, N. V., Review on exploration of graphene in the design and engineering of smart sensors, actuators and soft robotics. *Chemical Engineering Journal Advances* **2020,** *4*, 100034.
17. Liu, P.; Liu, A. T.; Kozawa, D.; Dong, J.; Yang, J. F.; Koman, V. B.; Saccone, M.; Wang, S.; Son, Y.; Wong, M. H.; Strano, M. S., Autoperforation of 2D materials for generating two-terminal memristive Janus particles. *Nat. Mater.* **2018,** *17* (11), 1005-1012.
18. Kim, S. J.; Mondal, S.; Min, B. K.; Choi, C.-G., Highly Sensitive and Flexible Strain–Pressure Sensors with Cracked Paddy-Shaped MoS2/Graphene Foam/Ecoflex Hybrid Nanostructures. *ACS Appl. Mater. Interfaces* **2018,** *10* (42), 36377-36384.
19. Hwang, M. T.; Heiranian, M.; Kim, Y.; You, S.; Leem, J.; Taqieddin, A.; Faramarzi, V.; Jing, Y.; Park, I.; van der Zande, A. M.; Nam, S.; Aluru, N. R.; Bashir, R., Ultrasensitive detection of nucleic acids using deformed graphene channel field effect biosensors. *Nat. Commun.* **2020,** *11* (1), 1543.
20. Han, Y.; Liu, Y.; Han, L.; Lin, J.; Jin, P., High-performance hierarchical graphene/metal-mesh film for optically transparent electromagnetic interference shielding. *Carbon* **2017,** *115*, 34-42.
21. Liu, A. T.; Yang, J. F.; LeMar, L. N.; Zhang, G.; Pervan, A.; Murphey, T. D.; Strano, M., Autoperforation of Two-Dimensional Materials to Generate Colloidal State Machines Capable of Locomotion. *Faraday Discuss.* **2020**, in press. DOI: 10.1039/D0FD00030B
22. Won, S.; Jung, H.-J.; Kim, D.; Lee, S.-H.; Van Lam, D.; Kim, H.-D.; Kim, K.-S.; Lee, S.-M.; Seo, M.; Kim, D.-S.; Lee, H.-J.; Kim, J.-H., Graphene-based crack lithography for high-throughput fabrication of terahertz metamaterials. *Carbon* **2020,** *158*, 505-512.

23. Vicarelli, L.; Heerema, S. J.; Dekker, C.; Zandbergen, H. W., Controlling defects in graphene for optimizing the electrical properties of graphene nanodevices. *ACS Nano* **2015,** *9* (4), 3428-3435.
24. Mirabedini, A.; Ang, A.; Nikzad, M.; Fox, B.; Lau, K.-T.; Hameed, N., Evolving Strategies for Producing Multiscale Graphene-Enhanced Fiber-Reinforced Polymer Composites for Smart Structural Applications. *Advanced Science* **2020,** *7* (11), 1903501.
25. Jiang, D.-E.; Sumpter, B. G.; Dai, S., Unique chemical reactivity of a graphene nanoribbon's zigzag edge. *J. Chem. Phys.* **2007,** *126* (13), 134701.
26. Jiang, D.-E.; Cooper, V. R.; Dai, S., Porous graphene as the ultimate membrane for gas separation. *Nano Lett.* **2009,** *9* (12), 4019-4024.
27. Ockwig, N. W.; Nenoff, T. M., Membranes for hydrogen separation. *Chem. Rev.* **2007,** *107* (10), 4078-4110.
28. Caneva, S.; Gehring, P.; García-Suárez, V. M.; García-Fuente, A.; Stefani, D.; Olavarria-Contreras, I. J.; Ferrer, J.; Dekker, C.; van der Zant, H. S. J., Mechanically controlled quantum interference in graphene break junctions. *Nat. Nanotechnol.* **2018,** *13* (12), 1126-1131.
29. Fischbein, M. D.; Drndić, M., Electron beam nanosculpting of suspended graphene sheets. *Appl. Phys. Lett.* **2008,** *93* (11), 113107.
30. Ci, L.; Xu, Z.; Wang, L.; Gao, W.; Ding, F.; Kelly, K. F.; Yakobson, B. I.; Ajayan, P. M., Controlled nanocutting of graphene. *Nano Res.* **2008,** *1* (2), 116-122.
31. Campos, L. C.; Manfrinato, V. R.; Sanchez-Yamagishi, J. D.; Kong, J.; Jarillo-Herrero, P., Anisotropic etching and nanoribbon formation in single-layer graphene. *Nano Lett.* **2009,** *9* (7), 2600-2604.
32. Bertolazzi, S.; Brivio, J.; Kis, A., Stretching and breaking of ultrathin MoS2. *ACS Nano* **2011,** *5* (12), 9703-9709.
33. Zhang, P.; Ma, L.; Fan, F.; Zeng, Z.; Peng, C.; Loya, P. E.; Liu, Z.; Gong, Y.; Zhang, J.; Zhang, X.; Ajayan, P. M.; Zhu, T.; Lou, J., Fracture toughness of graphene. *Nat. Commun.* **2014,** *5*, 3782.
34. Zhang, J.; Xiao, J.; Meng, X.; Monroe, C.; Huang, Y.; Zuo, J.-M., Free folding of suspended graphene sheets by random mechanical stimulation. *Phys. Rev. Lett.* **2010,** *104* (16), 166805.
35. Chissoe, W. F.; Vezey, E. L.; Skvarla, J. J., Hexamethyldisilazane as a drying agent for pollen scanning electron microscopy. *Biotech. Histochem.* **1994,** *69* (4), 192-198.
36. Suk, J. W.; Kitt, A.; Magnuson, C. W.; Hao, Y.; Ahmed, S.; An, J.; Swan, A. K.; Goldberg, B. B.; Ruoff, R. S., Transfer of CVD-grown monolayer graphene onto arbitrary substrates. *ACS Nano* **2011,** *5* (9), 6916-6924.
37. Balandin, A. A.; Ghosh, S.; Bao, W.; Calizo, I.; Teweldebrhan, D.; Miao, F.; Lau, C. N., Superior thermal conductivity of single-layer graphene. *Nano Lett.* **2008,** *8* (3), 902-907.
38. Bao, W.; Miao, F.; Chen, Z.; Zhang, H.; Jang, W.; Dames, C.; Lau, C. N., Controlled ripple texturing of suspended graphene and ultrathin graphite membranes. *Nat. Nanotechnol.* **2009,** *4* (9), 562-566.
39. van der Zande, A. M.; Barton, R. A.; Alden, J. S.; Ruiz-Vargas, C. S.; Whitney, W. S.; Pham, P. H. Q.; Park, J.; Parpia, J. M.; Craighead, H. G.; McEuen, P. L., Large-Scale Arrays of Single-Layer Graphene Resonators. *Nano Lett.* **2010,** *10* (12), 4869-4873.
40. Takamura, M.; Hibino, H.; Yamamoto, H., Applying strain into graphene by SU-8 resist shrinkage. *J. Phys. D Appl. Phys.* **2016,** *49* (28), 285303.
41. Ferrari, A. C.; Meyer, J. C.; Scardaci, V.; Casiraghi, C.; Lazzeri, M.; Mauri, F.; Piscanec, S.; Jiang, D.; Novoselov, K. S.; Roth, S.; Geim, A. K., Raman spectrum of graphene and graphene layers. *Phys. Rev. Lett.* **2006,** *97* (18), 187401.
42. Ferrari, A. C.; Basko, D. M., Raman spectroscopy as a versatile tool for studying the properties of graphene. *Nat. Nanotechnol.* **2013,** *8* (4), 235-246.
43. Tian, H.; Yang, Y.; Xie, D.; Ren, T.-L.; Shu, Y.; Sun, H.; Zhou, C.-J.; Liu, X.; Tao, L.-Q.; Ge, J.; Zhang, C.-H.; Zhang, Y., Laser directed lithography of asymmetric graphene ribbons on a polydimethylsiloxane trench structure. *Phys. Chem. Chem. Phys.* **2013,** *15* (18), 6825-6830.
44. Schedin, F.; Geim, A. K.; Morozov, S. V.; Hill, E. W.; Blake, P.; Katsnelson, M. I.; Novoselov, K. S., Detection of individual gas molecules adsorbed on graphene. *Nat. Mater.* **2007,** *6* (9), 652-655.
45. Reserbat-Plantey, A.; Kalita, D.; Han, Z.; Ferlazzo, L.; Autier-Laurent, S.; Komatsu, K.; Li, C.; Weil, R.; Ralko, A.; Marty, L.; Guéron, S.; Bendiab, N.; Bouchiat, H.; Bouchiat, V., Strain superlattices and macroscale suspension of graphene induced by corrugated substrates. *Nano Lett.* **2014,** *14* (9), 5044-5051.
46. Ferrari, A. C., Raman spectroscopy of graphene and graphite: Disorder, electron–phonon coupling, doping and nonadiabatic effects. *Solid State Commun.* **2007,** *143* (1), 47-57.
47. Mohiuddin, T. M. G.; Lombardo, A.; Nair, R. R.; Bonetti, A.; Savini, G.; Jalil, R.; Bonini, N.; Basko, D. M.; Galiotis, C.; Marzari, N.; Novoselov, K. S.; Geim, A. K.; Ferrari, A. C., Uniaxial strain in graphene by Raman spectroscopy: G peak splitting, Grüneisen parameters, and sample orientation. *Phys. Rev. B* **2009,** *79* (20), 205433.
48. Zan, R.; Bangert, U.; Ramasse, Q.; Novoselov, K. S., Metal−Graphene Interaction Studied via Atomic Resolution Scanning Transmission Electron Microscopy. *Nano Lett.* **2011,** *11* (3), 1087-1092.

49. Zan, R.; Bangert, U.; Ramasse, Q.; Novoselov, K. S., Evolution of gold nanostructures on graphene. *Small* **2011,** *7* (20), 2868-2872.
50. Lee, K. Y.; LaBianca, N.; Rishton, S. A.; Zolgharnain, S.; Gelorme, J. D.; Shaw, J.; Chang, T. H.-P., Micromachining applications of a high resolution ultrathick photoresist. *J. Vac. Sci. Technol. B* **1995,** *13* (6), 3012-3016.
51. Shaw, J. M.; Gelorme, J. D.; LaBianca, N. C.; Conley, W. E.; Holmes, S. J., Negative photoresists for optical lithography. *IBM J. Res. Dev.* **1997,** *41* (1.2), 81-94.
52. Lorenz, H.; Despont, M.; Fahrni, N.; LaBianca, N.; Renaud, P.; Vettiger, P., SU-8: a low-cost negative resist for MEMS. *J. Micromech. Microeng.* **1997,** *7* (3), 121.
53. Wong, W. H.; Pun, E. Y. B., Exposure characteristics and three-dimensional profiling of SU8C resist using electron beam lithography. *J. Vac. Sci. Technol. B* **2001,** *19* (3), 732-735.
54. Nallani, A. K.; Park, S. W.; Lee, J. B., Characterization of SU-8 as a resist for electron-beam lithography. In *Smart Sensors, Actuators, and MEMS*, 2003; Vol. 5116, pp 414-423.
55. Bilenberg, B.; Jacobsen, S.; Schmidt, M. S.; Skjolding, L. H. D.; Shi, P.; Bøggild, P.; Tegenfeldt, J. O.; Kristensen, A., High resolution 100 kV electron beam lithography in SU-8. *Microelectron. Eng.* **2006,** *83* (4-9), 1609-1612.
56. Cremers, C.; Bouamrane, F.; Singleton, L.; Schenk, R., SU-8 as resist material for deep X-ray lithography. *Microsyst. Technol.* **2001,** *7* (1), 11-16.
57. Teh, W. H.; Dürig, U.; Drechsler, U.; Smith, C. G.; Güntherodt, H. J., Effect of low numerical-aperture femtosecond two-photon absorption on (SU-8) resist for ultrahigh-aspect-ratio microstereolithography. *J. Appl. Phys.* **2005,** *97* (5), 054907.
58. Schrader, P. G. Polyglycidyl ethers of branched novolacs. 4474929, 1984/10/2, 1984.
59. Ceyssens, F.; Puers, R., SU-8 Photoresist. *Encyclopedia of Nanotechnology* **2016**, 3858-3873.
60. Sarkar, M.; Mohapatra, Y. N., Electron beam lithography in thick negative tone chemically amplified resist: Controlling sidewall profile in deep trenches and channels. *Microelectron. Eng.* **2014,** *130*, 1-7.
61. Dubonos, S. V.; Gaifullin, B. N.; Raith, H. F.; Svintsov, A. A.; Zaitsev, S. I., Evaluation, verification and error determination of proximity parameters α, β and ν in electron beam lithography. *Microelectron. Eng.* **1993,** *21* (1), 293-296.
62. Glezos, N.; Patsis, G. P.; Raptis, I.; Argitis, P.; Gentili, M.; Grella, L., Application of a reaction-diffusion model for negative chemically amplified resists to determine electron-beam proximity correction parameters. *J. Vac. Sci. Technol. B* **1996,** *14* (6), 4252-4256.
63. Denning, R. G.; Blanford, C. F.; Urban, H.; Bharaj, H.; Sharp, D. N.; Turberfield, A. J., The Control of Shrinkage and Thermal Instability in SU-8 Photoresists for Holographic Lithography. *Adv. Funct. Mater.* **2011,** *21* (9), 1593-1601.
64. Ross, P. J., *Taguchi techniques for quality engineering: loss function, orthogonal experiments, parameter and tolerance design*. McGraw-Hill New York: 1988.
65. Roy, R. K., *A Primer on the Taguchi Method*. Society of Manufacturing Engineers: 1990; p 247.
66. Lawson, R. A.; Tolbert, L. M.; Younkin, T. R.; Henderson, C. L., Negative-tone molecular resists based on cationic polymerization. In *Advances in Resist Materials and Processing Technology XXVI*, International Society for Optics and Photonics: 2009; Vol. 7273, p 72733E.
67. Ling, Z. G.; Lian, K.; Jian, L., Improved patterning quality of SU-8 microstructures by optimizing the exposure parameters. In *Advances in Resist Technology and Processing XVII*, International Society for Optics and Photonics: 2000; Vol. 3999, pp 1019-1027.
68. Kawamura, Y.; Toyoda, K.; Namba, S., Deep uv submicron lithography by using a pulsed high-power excimer laser. *J. Appl. Phys.* **1982,** *53* (9), 6489-6490.
69. Zhang, Z.; Zhang, X.; Wang, Y.; Wang, Y.; Zhang, Y.; Xu, C.; Zou, Z.; Wu, Z.; Xia, Y.; Zhao, P.; Wang, H. T., Crack Propagation and Fracture Toughness of Graphene Probed by Raman Spectroscopy. *ACS Nano* **2019,** *13* (9), 10327-10332.

For Table of Contents Only

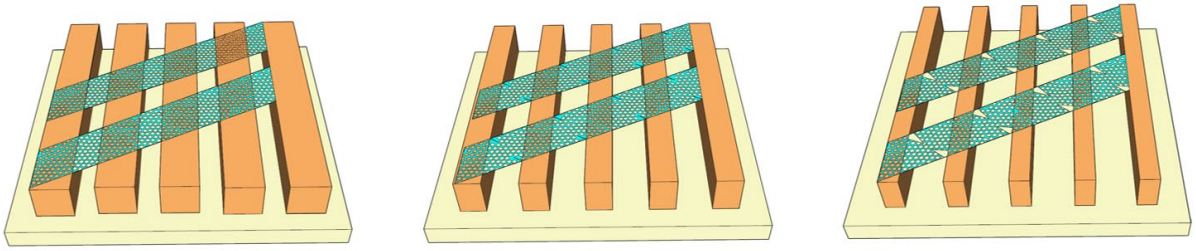

Supporting Information

Controlled Nanoscale Cracking of Graphene Ribbons by Polymer Shrinkage

Anjishnu Sarkar,[†] Debadrita Paria,[‡] Ishan Barman,[‡,†,▽] David H. Gracias[†, ||, §*]

[†]Department of Chemical and Biomolecular Engineering, Johns Hopkins University. 3400 North Charles Street, Baltimore, MD 21218, United States.
[‡]Department of Mechanical Engineering, Johns Hopkins University. 3400 North Charles Street, Baltimore, MD 21218, United States.
[||] Department of Materials Science and Engineering, Johns Hopkins University. 3400 North Charles Street, Baltimore, MD 21218, United States.
[§]Department of Chemistry, Johns Hopkins University. 3400 North Charles Street, Baltimore, MD 21218, United States.
[†]Department of Oncology and [▽]The Russell H. Morgan Department of Radiology and Radiological Science, The Johns Hopkins University School of Medicine, Baltimore, Maryland 21287, United States
*Corresponding author: dgracias@jhu.edu

1. Fabrication and patterning schematics

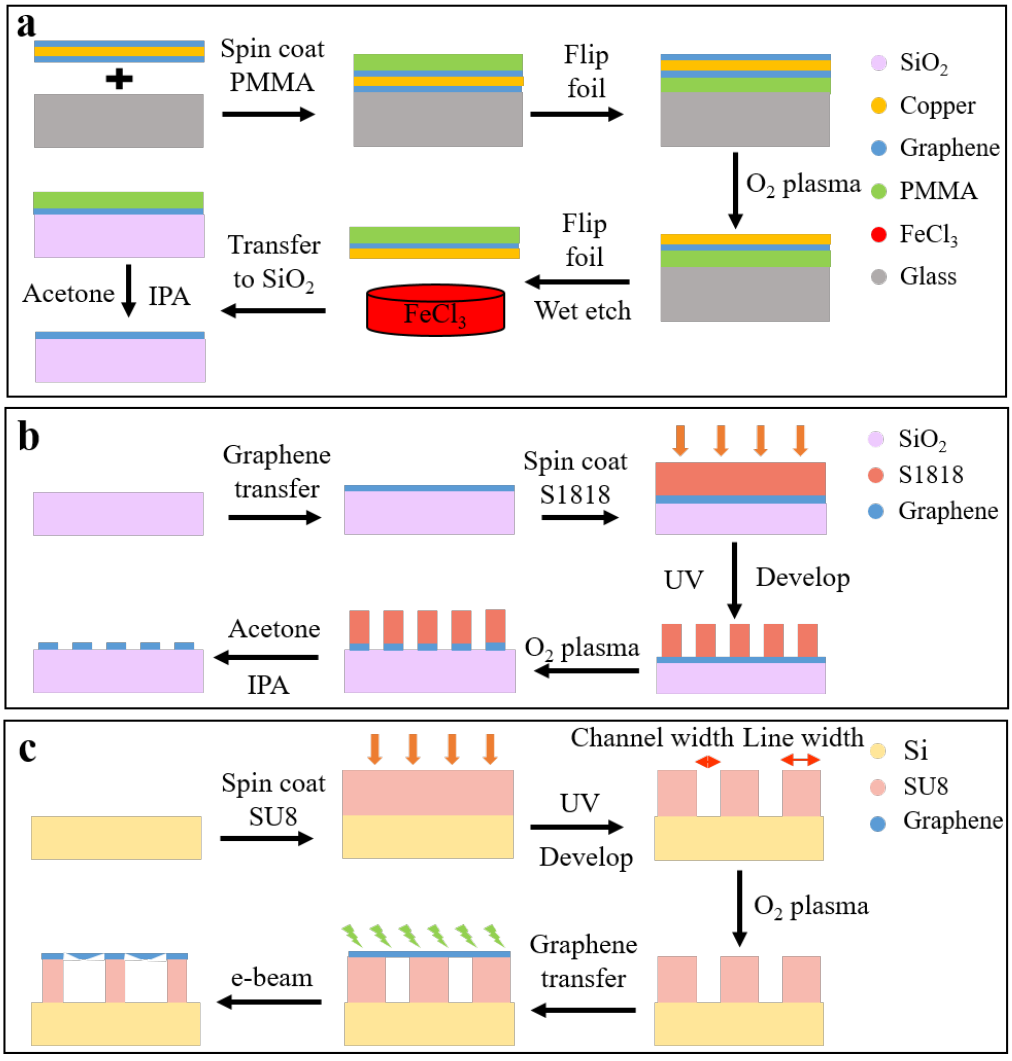

Figure S1. Schematics of, (a) PMMA assisted wet transfer of CVD graphene from copper to the SiO_2 surface. (b) Micropatterning of graphene on a SiO_2 substrate. (c) Transfer of patterned graphene microribbons on SU8 lines followed by e-beam mediated shrinkage of SU8 lines, expansion of SU8 channel width and breakage of graphene microribbons.

2. Crack-free, suspended graphene microribbons after transfer on micropatterned SU8 lines

We patterned 3 μm wide graphene ribbons and subsequently transferred them on SU8 lines in an oblique fashion (Figure S2(a)). We used scanning electron microscopy at a low probe current and at a tilt angle of 30° to ensure that graphene ribbons did not crack prior to controlled breakage at a higher probe current (Figure S2(b)). The Raman spectra of the suspended graphene ribbons show the signature of crack-free graphene and the defect peak (D) at 1350 cm^{-1} is absent (Figure S2(c)).

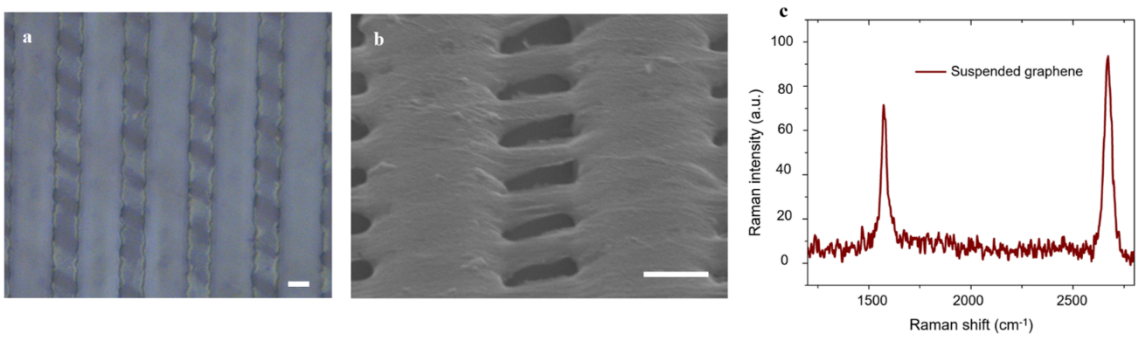

Figure S2. Micrographs of micropatterned graphene ribbons before cracking (a) Bright field optical micrograph of 3 μm wide graphene ribbons suspended on 8 μm wide SU8 lines (b) Isometric SEM micrographs of crack-free, suspended ribbons taken at an angle of 30°. The scale bar is 4 μm. (c) Raman spectra of crack-free, suspended graphene microribbons on SU8.

3. Determination of the best permutation for achieving highest SU8 channel width

The rise in the spacing between two adjacent SU8 lines (channel width) is a latent parameter that is directly proportional to the extent of breakage in graphene. The SU8 channel width is governed by three factors, namely UV crosslinking intensity, temperature, and e-beam dose. To better understand the effect of each of the aforementioned factors on SU8 channel width, we carried out 3^3=27 experiments, which correspond to 27 unique permutations. Each experiment was conducted in triplicates, and we report the average value of SU8 channel width (listed as Table S1). We observe that the channel width attains its minimum value for a UV crosslinking intensity of 125 mJ/cm^2 and a low e- beam dose (experiments 19 and 25). The SU8 channel width reaches its highest value for UV crosslinking intensity of 50 mJ/cm^2 and a high e-beam dose (experiment 6). This shows that SU8 channel width increases with e-beam dose and decreases with UV crosslinking.

Table S1. Evolution of SU8 channel width for 27 permutations of UV crosslinking intensity, Temperature and e-beam dose.

Experiment	UV crosslinking intensity (mJ/cm^2)	Temperature (°C)	e-beam dose (a.u.)	SU8 channel width (μm)
1	50	No heating	Low	6.7
2	50	No heating	Med	6.8
3	50	No heating	High	7.8
4	50	90	Low	8.7
5	50	90	Med	9.0
6	50	90	High	9.5
7	50	200	Low	7.7
8	50	200	Med	8.1
9	50	200	High	8.5
10	85	No heating	Low	7.3
11	85	No heating	Med	7.9
12	85	No heating	High	8.3
13	85	90	Low	7.7
14	85	90	Med	8.3
15	85	90	High	8.8
16	85	200	Low	8.0
17	85	200	Med	8.1
18	85	200	High	8.3
19	125	No heating	Low	5.2
20	125	No heating	Med	5.6
21	125	No heating	High	5.9
22	125	90	Low	5.5
23	125	90	Med	6.1
24	125	90	High	6.7
25	125	200	Low	5.3
26	125	200	Med	5.7
27	125	200	High	6.0

4. Determination of the absorption current corresponding to the e-beam doses "low", "med" and "high" using a Faraday cup

We measured the approximate values of the three distinct e-beam doses as follows. All our e-beam experiments on e-beam induced SU8 shrinkage were conducted using a tungsten filament thermionic emission JEOL JSM IT100 SEM. Since it was not readily possible to install a Faraday cup on this SEM, we also reproduced the SU8 shrinkage experiments using a Thermo Scientific Helios G4 UC Focused Ion Dual Beam instrument which consists of an e-beam for SEM. We installed a Faraday cup to the latter. To ensure reproducibility, we irradiated SU8 lines UV crosslinked with 80 mJ/cm^2 with the e-beam at different probe currents, as measured by the Faraday cup (Figure S3). We maintained the identical working distance (11 mm), magnification (6000X) and acceleration voltage (20 kV) as the original experiments. For each probe current, we increased the duration of exposure to match the rise in SU8 channel width as obtained with each of "low", "med", and "high" e-beam doses. Listed below are the charge per unit area values of the e-beam doses.

Low e-beam dose: Charge per unit area < 0.5 mC/cm^2

Med e-beam dose: Charge per unit area ~ 366.1 mC/cm^2

High e-beam dose: Charge per unit area > 915.1 mC/cm^2

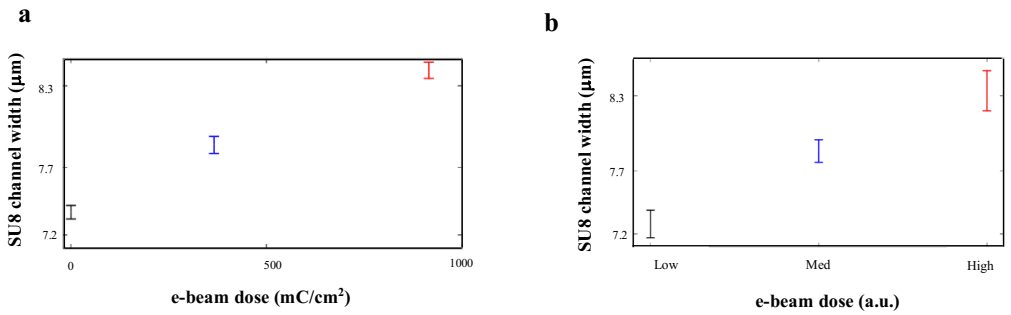

Figure S3. Identification of the e-beam doses which results in identical increase in SU8 channel width for resist photocrosslinked with 85 mJ/cm^2. (a) Variation of SU8 channel width with e-beam dose measured with a Faraday cup in mC/cm^2. (b) Variation of SU8 channel width at different e-beam dose

5. Effect of e-beam dose on 5 μm wide graphene microribbons

We repeated the fabrication corresponding to Figure 2, and irradiated the samples at the three e-beam doses (Figure S4 (d-f)). We observed the formation of a narrow slit for the med e-beam dose, followed by a widening of the slit at the high e-beam dose.

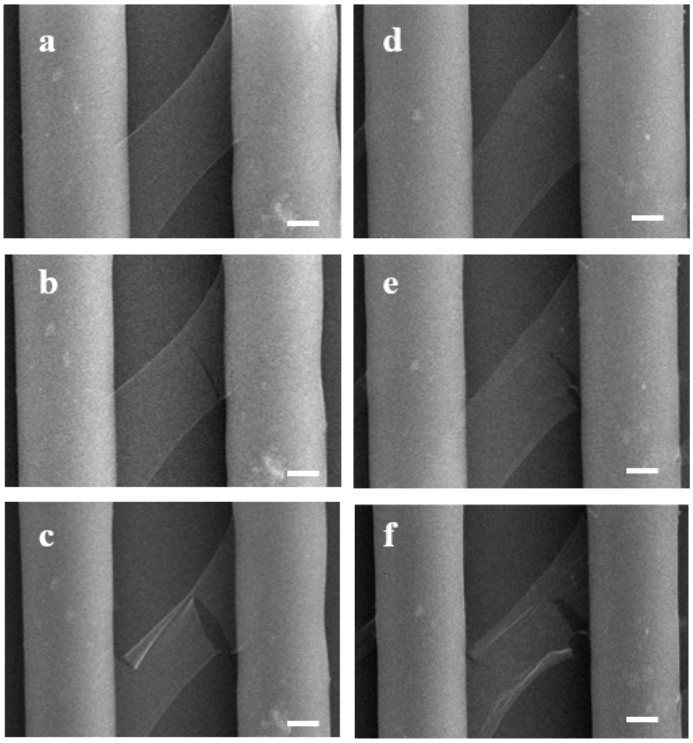

Figure S4. Evolution of rise in SU8 channel width and consequent breakage of graphene microribbons. SEM micrographs showing progressive stages of graphene breakage for microribbon 1 (a-c) and microribbons 2 (d-f). The scale bar is 2 μm.

6. Control experiments: Expansion of the SU8 channel width in the absence of graphene

We patterned SU8 channels with a channel width of 6.4 µm (Figure S5 (a)) and subjected them to e-beam irradiation. At medium e-beam dose, the channel width increases to 7 µm and remains constant at high e-beam dose.

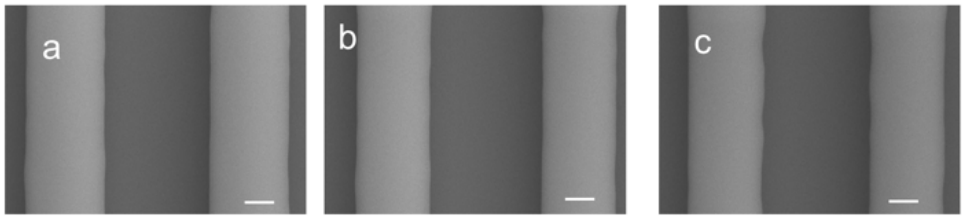

Figure S5. SEM micrographs of a SU8 channel before and after irradiation with the e-beam (a) SU8 at low e-beam dose (b) medium e-beam dose. (c) high e-beam dose. The scale bar is 2 µm.

7. Nanoscale cracks developed in 8 µm wide, suspended graphene microribbons

We patterned 8 µm wide graphene ribbons with 5 µm spacing and subsequently transferred them on SU8 lines in an oblique fashion (Figure S6 (a)). At medium e-beam dose, a narrow slit forms (Figure S6 (b)), which assumes a length of 400 nm upon irradiation with the high e-beam dose (Figures S6 (c) and (d)).

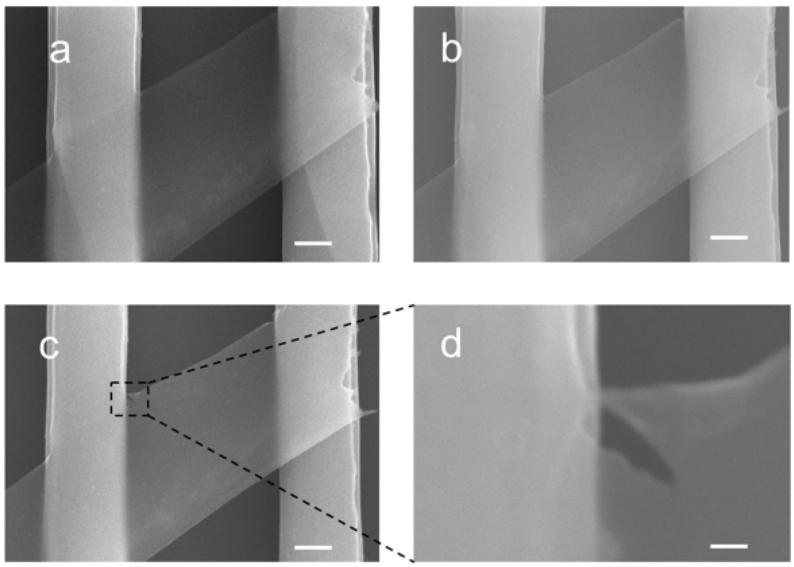

Figure S6. SEM micrographs of 8 µm wide graphene microribbons before and after cracking (a) SEM showing supported and suspended regions (b) SEM of suspended graphene at medium e-beam dose. (c) 200 nm crack at the intersection of suspended graphene and SU8 at high e-beam dose. (d) Zoomed in image of graphene and SU8. The scale bar is 2 µm for a-c and 200 nm for d.

8. Note on the spread in the standard deviation of the response parameter

The spread in the standard deviations for Figure 3a and Figure 4a can be attributed to two reasons. First, to discretize the effect of each factor for one of three levels, we choose the permutations which correspond to a distinct level for a given factor. Hence, the mean value for a factor at a level is governed by several permutations of the other two factors across different levels, which causes the standard deviation to be high. Secondly, as shown in Figure 2a, upon increasing the e-beam dose from medium to high, the length of the nanoscale crack remains constant while the area of the cracks increases by a factor of seven. Since the percentage of graphene cracking is measured as the ratio of the cracked slit length to the original ribbon width (5μm), the increase in area is not accounted for in the percentage cracking. This causes the standard deviation to assume negative percentages in Figure 4a. However, we calculate the signal-to-noise (S/N) ratios for the response parameters across the levels to gain a better insight of the robustness of the DOE.[1] We show in Figures 5 and 6 that the UV crosslinking plays a dominant role in the widening of SU8 channels, and the consequent breakage of graphene microribbons.

9. Note on Video S1

Video S1 is a video showing the *in situ*, complete breakage of a suspended graphene microribbon in real time, taken in an SEM. The SU8 lines were photopatterned with a UV crosslinking intensity of 125 mJ/cm^2 and annealed on a hotplate at 90 °C prior to the transfer of the graphene microribbon. The SU8 lines have a width of 7.6±0.1 μm, and a channel width of 5.8±0.0 μm. We observe that a crack appears in the graphene microribbon in approximately 45 seconds (which corresponds to an e-beam dose between 0.5 mC/cm^2 and 27.4 mC/cm^2), and the graphene microribbon cracks completely in approximately 58 seconds (which corresponds to an e-beam dose between 27.4 mC/cm^2 and 35.3 mC/cm^2).

REFERENCES

1. Mahapatra, S. S.; Chaturvedi, V., Modelling and analysis of abrasive wear performance of composites using Taguchi approach, *Int. J. Eng. Sci. Technol.*, **2009**, 1(1) 123-135.